INTERNATIONAL JOURNAL FOR NUMERICAL METHODS IN ENGINEERING
Int. J. Numer. Meth. Engng 2002; **53**:2117–2142 (DOI: 10.1002/nme.374)

A simple algorithm for localized construction of non-matching structural interfaces

K. C. Park, C. A. Felippa*,† and G. Rebel

Department of Aerospace Engineering Sciences and Center for Aerospace Structures, University of Colorado, Campus Box 429, Boulder, CO 80309, U.S.A.

SUMMARY

A simple and effective algorithm for the modular construction of non-matched interfaces is presented for the partitioned solution of large-scale structural problems. The formulation is based on a recently developed four-field variational principle, which introduces a connection frame between the interfaced partitions. A key result of the present study is a frame nodal placement criterion that uniquely determines the frame discretization into piecewise linear elements so that the interface patch test condition is satisfied *a priori*. The method is demonstrated with several 2D and 3D example problems. Copyright © 2002 John Wiley & Sons, Ltd.

KEY WORDS: non-matching grids; interface patch test; localized Lagrange multipliers; partitioned analysis; four-field variational principle; interface frame concept

1. INTRODUCTION

The interface coupling of independently discretized finite element models is emerging as a key technology in support of efficient parallel computations, local mesh generation and refinement, contact-impact problems, and multiphysics simulations. Interfaced meshes are called *matching* if interface nodes and degrees of freedom therein coincide, and element boundary motions conform. In this case, the interface kinematic compatibility conditions are straightforward to construct and enforce. If node locations do not coincide, degrees of freedom do not agree, or boundary motions are non-conforming, the discretizations are said to be *non-matching*. Both "partition" and "subdomain" will be indistinctly used here to denote interfaced discretizations, although those two terms have physical and mathematical connotation, respectively.

*Correspondence to: C. A. Felippa, Department of Aerospace Engineering Sciences and Center for Aerospace Structures, University of Colorado, Campus Box 429, Boulder, CO 80309, U.S.A.
† E-mail: carlos.felippa@colorado.edu

Contract/grant sponsor: Lawrence Livermore National Laboratory; contract/grant number: B347880
Contract/grant sponsor: Sandia National Laboratories; contract/grant number: AS-5666
Contract/grant sponsor: National Science Foundation; contract/grant number: ECS-9725504

Received 24 December 2000
Revised 20 April 2001

Non-matching meshes arise in practice because of physical, modelling or computational reasons. Three examples: components of the complete structure are discretized by separate teams using different programs and mesh-generation tools; meshes are independently refined to capture local or multiscale behaviour; or partitions are highly heterogeneous as in foam surrounding a payload. In contact-impact problems, non-matching interfaces arise naturally on account of physics. Methods for coupling non-matching meshes include primal and dual methods. The latter introduce Lagrange multipliers as independent variables that physically represent interaction forces or fluxes. This is the approach followed here.

The classical method of Lagrange multipliers [1] links the partition-boundary displacements of a subdomain to those of interfacing subdomains. Interface compatibility conditions thus derived are scaled by a corresponding Lagrange multiplier, giving rise to a constraint functional. The total system energy functional is then obtained by adding the interface constraint functional to the free energy of unconnected subdomains. Since in mechanics it involves the displacements of the partitioned subdomains and the Lagrange multipliers, it is also called a two-field formulation. Applications of two-field formulations to contact problems may be found in References [2–5], among others.

Three-field formulations introduce interface displacements as an independently varied field. These have been studied for interface modelling in the context of local–global FEM analysis by Aminpour *et al.* [6, 7] and for mathematical analysis of FEM approximations by Brezzi and Marini [8]. Much recent work concerns the mortar method, which begins with a three-field formulation where the third field is eliminated upon construction of the interface approximations. This approach is extensively studied in References [9, 10]

From a practical viewpoint, an interface discretization method that preserves the patch test passing features of individual subdomains would be extremely useful. This has been the focus of recent work in contact problems by Taylor and Papadopoulos [4] and Crisfield [5], who identified geometric gaps and interface force lumping as major sources of errors in passing the test over contact interfaces. A key objective of the present paper is to develop an interface patch test criterion that can be employed *a priori* for the localized construction of non-matching structural interfaces. It should be noted that, with the notable exception of the Free Formulation of Bergan and Nygård [11], the patch test has been used for *a posteriori* evaluation after elements are constructed, rather than as a discretization design tool.

The theoretical foundation of the present study is a four-field variational principle [12, 13] whose variables consist of subdomain deformation modes, Lagrange multipliers independently defined along subdomain interfaces, displacements of a frame interposed between subdomains, and self-equilibrium modes of the frame and subdomains. The two key features of this variational framework that are pertinent to our stated objective are: (i) the introduction of the frame that localizes the Lagrange multipliers (interface forces); and (ii) the global self-equilibrium of the frame verified through its rigid-body motions as test functions. It will be shown that (i) leads to a modular construction of interface constraints. If the frame displacement field is piecewise linear (ii) provides a frame node placement criterion that determines the frame node locations so that the interface patch test condition is satisfied *a priori*.

The remainder of the paper is organized as follows. Section 2 reviews the underlying four-field variational formulation. Section 3 examines the interpolation schemes adopted for the localized multipliers and derives the frame node placement criterion, which is a key contribution of the present study. Once the frame nodal points are determined, the frame interpolation follows by using the frame discrete nodes. Illustrative examples of frame node

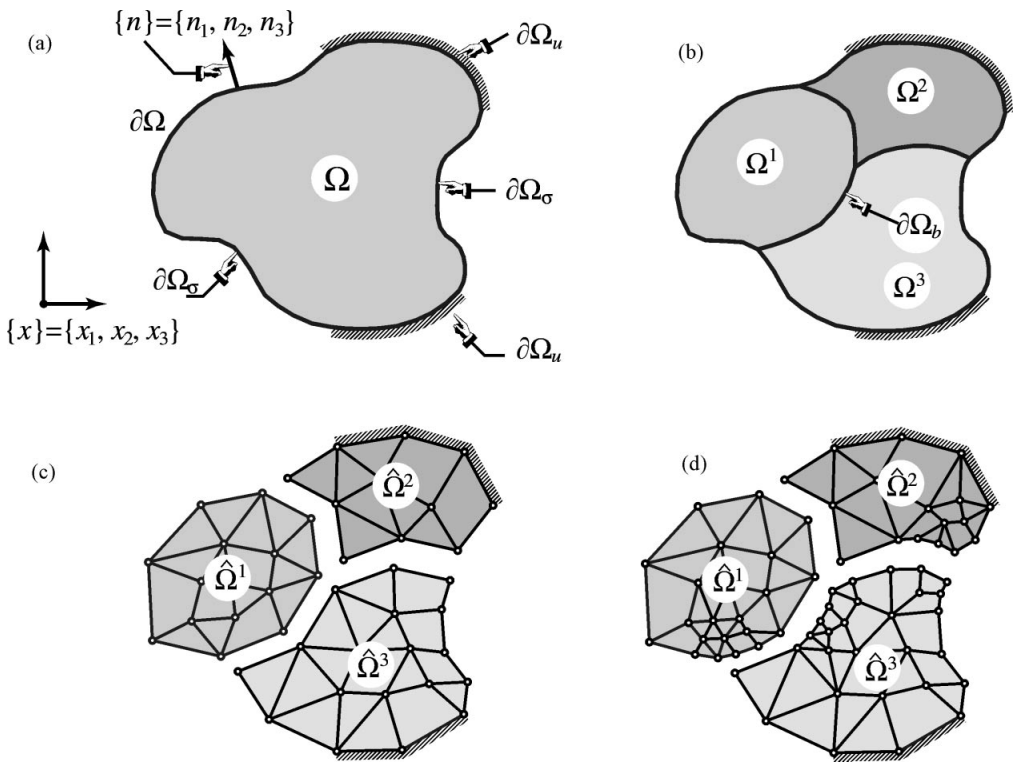

Figure 1. (a) A domain Ω with boundary $\partial\Omega = \partial\Omega_\sigma \cup \partial\Omega_u$; (b) partition into three subdomains: Ω^1, Ω^2 and Ω^3 by cutting it through interface $\partial\Omega_b$. Two FEM discretizations of (b): (c) matching submeshes; (d) non-matching submeshes. Superposed hats distinguish discrete versions.

placement are shown in Section 4. These are followed by numerical examples verifying the interface patch test. Finally we summarize our results and comment on the connection of the present formulation to the master–slave approach currently used in commercial FEM codes.

2. REVIEW OF GOVERNING VARIATIONAL PRINCIPLE

This section is a streamlined review, combining statics and dynamics, of a lenghtier expository presentation [13]. Consider the elastic body illustrated in Figures 1 and 2. The body of Figure 1(a) occupies domain Ω, which is referred to a Cartesian system x_i. The boundary $\partial\Omega$ has exterior normal n_i. For illustration the domain is partitioned into three subdomains Ω^1, Ω^2 and Ω^3 as depicted in Figures 1(b)–1(d). An internal boundary $\partial\Omega_b$ called a *interface frame* or simply *frame*, is placed as shown in Figure 2(b). The displacements of $\partial\Omega_b$ are varied independently from those of the subdomains. The partition frame is "glued" to the adjacent subdomains by Lagrange multiplier fields λ_ℓ, as shown in Figures 2(c) and (d). These multipliers are said to be *localized* because they are associated with specific subdomains.

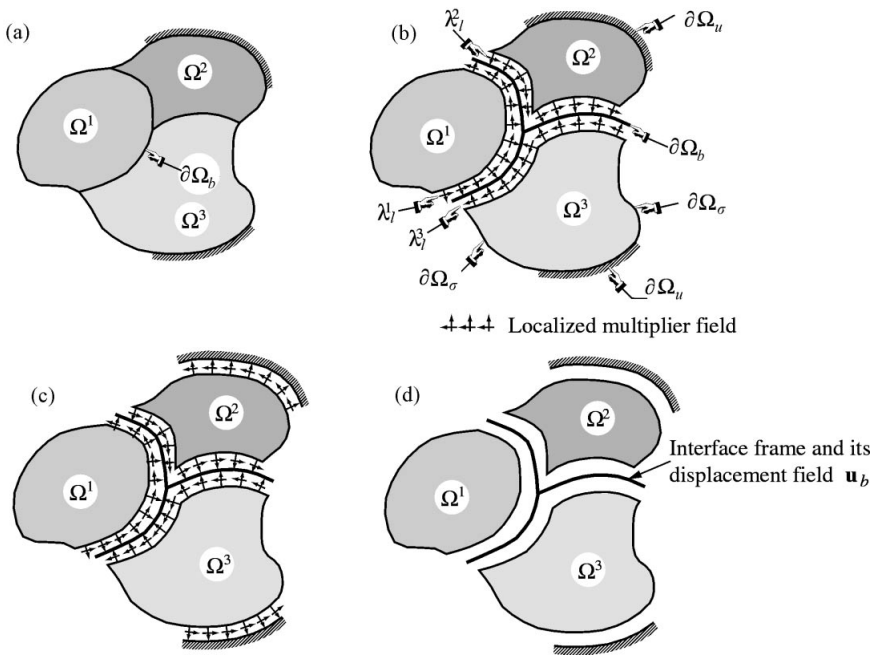

Figure 2. Interface treatment for functional construction: (a) the domain of Figure 1(a) divided into three subdomain partitions; (b) functional Π_{HWM2}: linkup by localized multipliers and connection frame; (c) functional Π_{PEM2}: multipliers are extended to include prescribed-displacement portions $\partial\Omega_u$; (d) the subdomain connection frame with its own independently varied displacement field.

The interior fields of subdomain Ω^m, considered as an isolated entity, are: displacements u_i^m, strain ε_{ij}^m, stress σ_{ij}^m and d'Alembert force $\bar{f}_i^m = f_{ii}^m - \rho_i^m \ddot{u}_i^m$, where ρ_i^m is the density of the material and $\ddot{u}_i^m$ denotes material acceleration. The boundary $\partial\Omega^m$ can be generally decomposed into $\partial\Omega_u^m$, $\partial\Omega_\sigma^m$ and $\partial\Omega_b^m$. $\partial\Omega_u^m$ and $\partial\Omega_\sigma^m$ are portions of $\partial\Omega^m$ where displacements $\bar{u}_i$ and tractions $\bar{t}_i$, respectively, are prescribed. $\partial\Omega_b^m$ is the interface with other subdomains, over which the Lagrange multiplier field $\lambda_{\ell i}^m$ has the role of surface traction. Subdomain linking is done through the displacement u_{bi} of the partition frame $\partial\Omega_b$. The strain energy density and symmetric displacement gradients are denoted by

$$\mathscr{U}(\varepsilon_{ij}) = \tfrac{1}{2} E_{ijkl}\varepsilon_{ij}\varepsilon_{kl}, \quad \varepsilon_{ij} = \tfrac{1}{2}(u_{i,j} + u_{j,i}) \tag{1}$$

respectively, in which E_{ijkl} are the elastic moduli, commas denote partial derivatives, and the summation convention is in effect. With these ingredients in place, a three-field functional for linear elastodynamics can be presented as a sum of subdomain contributions:

$$\Pi_{\mathrm{PEM2}}(u_i, \lambda_{\ell i}, u_{bi}) = \Pi_{\mathrm{PE}} - \pi_u = \sum_m \Pi_{\mathrm{PE}}^m - \sum_m \pi_u^m \tag{2}$$

in which

$$\Pi_{\mathrm{PE}}^{m} = \int_{\Omega^m} [\mathscr{U}(u_i^m) - u_i^m \bar{f}_i^m]\,\mathrm{d}\Omega - \int_{\partial\Omega_\sigma^m} u_i^m \bar{t}_i^m\,\mathrm{d}S$$
$$\pi_u^m = \int_{\partial\Omega_b^m \cup \partial\Omega_u^m} \lambda_{\ell i}^m (u_i^m - u_{bi})\,\mathrm{d}S \tag{3}$$

In the above equation, the sum over m extends from 1 to the number of subdomains N_{s}. For the boundary integrals $\mathrm{d}S$ is used to denote the boundary differential instead of the clumsier $\mathrm{d}\partial\Omega$. The only inter-partition connection is through u_{bi} in π_u^m, which is called an *interface potential* or *dislocation potential* in continuum mechanics. The sum of the π_u^m results in the integral being carried out twice over each interface, once on each side of $\partial\Omega_b$. It should be noted that variants of the preceding functional were proposed and studied by Atluri [14], Tong [15], and Felippa [16, 17] for the construction of hybrid finite elements for which the interior displacements u_i and interface forces $\lambda_{\ell i}$ are eliminated at the element level.

For several applications of partitioned analysis such as inverse problems and parallel solution, it has been found convenient to explicitly separate the rigid-body modes in the governing equation of floating subdomains. Following Fraeijs de Veubeke [18, 19] this can be accomplished by decomposing the total displacements into deformational and rigid-body components, i.e., $d_i(x_k)$ and $r_i(x_k)$, respectively:

$$u_i(x_k) = d_i(x_k) + r_i(x_k) \quad \text{such that} \quad \int_{\Omega^m} \rho^m d_i^m r_i^m\,\mathrm{d}\Omega = \int_{\Omega^m} \rho^m (u_i^m - r_i^m) r_i^m\,\mathrm{d}\Omega = 0 \tag{4}$$

Since $u_{(i,j)} = d_{(i,j)}$ the strain energy density $\mathscr{U}$ becomes function of the deformational displacements d_i only: $\mathscr{U}(d_i) = \frac{1}{2} E_{ijkl} d_{(i,j)} d_{(k,l)}$. Inserting (4) into (1) we obtain the four-field functional presented in Park and Felippa [13]

$$\Pi_{\mathrm{FF}}(d_i, r_i, \lambda_{\ell i}, u_{bi}) = \Pi_{\mathrm{PE}} - \pi_u = \sum_m \Pi_{\mathrm{PE}}^m - \sum_m \pi_u^m \tag{5}$$

in which

$$\Pi_{\mathrm{PE}} = \int_{\Omega^m} [\mathscr{U}(d_i^m) - (d_i^m + r_i^m)\bar{f}_i^m]\,\mathrm{d}\Omega - \int_{\partial\Omega_\sigma^m} (d_i^m + r_i^m)\bar{t}_i^m\,\mathrm{d}S$$
$$\pi_u^m = \int_{\partial\Omega_b^m} \lambda_{\ell i}^m (d_i^m + r_i^m - u_{bi})\,\mathrm{d}S \tag{6}$$

To carry out the variation of this functional we introduce the rigid-body displacements r_i^m of each partitioned subdomain, which can be expressed as

$$r_i^m = R_{ij}^m \alpha_j^m \tag{7}$$

where α_j^m are subdomain rigid-body mode (RBM) amplitudes and R_{ij}^m are entries of a dimensionless full-rank matrix $\mathbf{R}^m$ whose columns span the RBMs. The entries of $\mathbf{R}^m$ are at most linear in the co-ordinates x_i. $\mathbf{R}^m$ is formed by selecting a linearly independent RBM basis for its columns, followed by orthonormalization: $\int_{\Omega^m} R_{ji}^m R_{ik}^m = V^m \delta_{jk}$, in which δ_{jk} is the Kronecker delta and $V^m = \int_{\Omega^m} \mathrm{d}\Omega$ is the subdomain volume (area in 2D, length in 1D).

Substituting (7) into (5) and performing the first variation on the resulting functional leads to

$$\delta\Pi_{\mathrm{FF}}(d_i,\alpha_i,\lambda_{\ell i},u_{bi})=\sum_m\{G^m_{di}+G^m_{\alpha i}+G^m_{\lambda\ell i}+G^m_{ubi}\}$$

$$\begin{aligned}
G^m_{di} &= \int_{\Omega^m} p^m_i\delta d^m_i\,\mathrm{d}\Omega-\int_{\Omega^m}(f^m_i-\rho^m\ddot{d}^m_i)\delta d^m_i\,\mathrm{d}\Omega-\int_{\partial\Omega^m_\sigma}\bar{t}^m_i\delta d^m_i\,\mathrm{d}S\\
&\quad-\int_{\partial\Omega^m_b}\lambda^m_{\ell i}\delta d^m_i\,\mathrm{d}S\\
G^m_{\alpha i} &= -\int_{\Omega^m}(\bar{f}^m_j R^m_{ij}-\rho^m R^m_{ij}\ddot{\alpha}^m_j)\delta\alpha^m_i\,\mathrm{d}\Omega-\int_{\partial\Omega^m_\sigma}\bar{t}^m_j R^m_{ij}\delta\alpha^m_i\,\mathrm{d}S\\
&\quad-\int_{\partial\Omega^m_b}\lambda^m_{\ell i}R^m_{ij}\delta\alpha^m_i\,\mathrm{d}S\\
G^m_{\lambda\ell i} &= -\int_{\partial\Omega^m_b}[d^m_i+R^m_{ij}\alpha^m_j-u_{bi}]\delta\lambda^m_{\ell i}\,\mathrm{d}S\\
G^m_{ubi} &= -\int_{\partial\Omega^m_b}\lambda^m_{\ell i}\delta u_{bi}\,\mathrm{d}S
\end{aligned}\tag{8}$$

Here p^m_i is the internal force density that results from the variation of the internal energy density: $\delta\mathscr{U}^m=p^m_i\delta d^m_i$. Setting the variation (8) to zero provides weak forms of deformational equilibrium, rigid-body equilibrium, interface compatibility (including prescribed displacements) and interface equilibrium (Newton's third law at subdomain boundaries) conditions, respectively. The first two are *localized* at the subdomain level. The only connection between subdomains is done through the last two conditions, which bring in the partition frame displacements u_{bi}.

3. FRAME NODE PLACEMENT

As noted in the Introduction, non-matching meshes arise from many sources: separately constructed discretizations, localized mesh generation and refinement, global–local analysis and multiphysics problems. The functionals (2) and (5) provide adequate tools to treat non-matching meshes of mechanical finite elements. This section discusses the discretization procedure associated with the use of Lagrange multipliers. It should be noted that master–slave techniques have been developed to couple non-matching meshes, and are available in commercial FEM codes. Such techniques are appropriate when master and slaves interfaces can be readily identified; for example a fine mesh linked to a coarse one as common in global–local analysis.

For definiteness the discussion refers to the 2D configuration illustrated in Figure 3. Upon discretization the nodes on the connection frame $\partial\Omega_b$ match neither those on subdomain Ω^1 nor subdomain Ω^2. Throughout this section, the displacement field is kept as u_i, without decomposing into r_i and d_i, to clarify the exposition. The frame equilibrium operator G_{ubi}

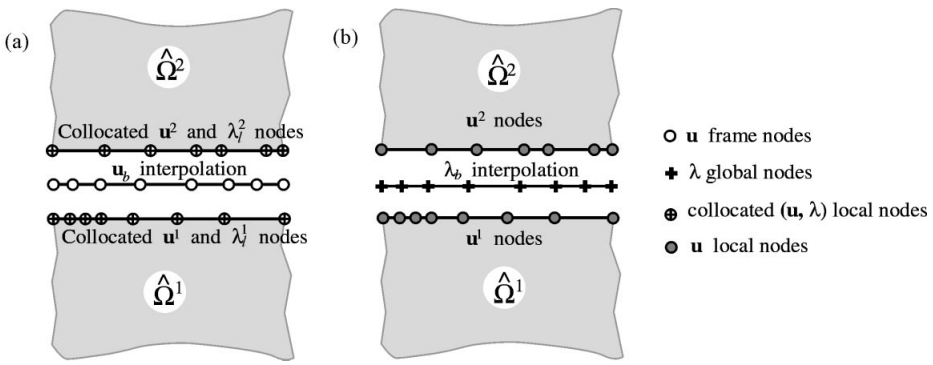

Figure 3. Two connection schemes for non-matched 2D mesh interfaces: (a) connection by frame (global) displacements and node-collocated local multipliers; (b) two-field connection by global multipliers.

derived in (8) for the two-partition problem illustrated in Figure 3(a) is given by

$$G_{ubi}(\lambda^1_{\ell i}, \lambda^2_{\ell i}, \delta u_{bi}) = \int_{\partial\Omega^1_b} \lambda^1_{\ell i} \delta u_{bi}\, \mathrm{d}S + \int_{\partial\Omega^2_b} \lambda^2_{\ell i} \delta u_{bi}\, \mathrm{d}S \tag{9}$$

In the above expression, $\partial\Omega^1_b$ denotes the projection of attributes of $\partial\Omega^1$ onto $\partial\Omega_b$, and similarly for $\partial\Omega^2_b$.

The FEM interpolations assumed for the configuration of Figure 3(a) are

$$\{\lambda^1\} = \mathbf{N}^1_\lambda \boldsymbol{\lambda}^1, \quad \{\lambda^2\} = \mathbf{N}^2_\lambda \boldsymbol{\lambda}^2, \quad \{u_b\} = \mathbf{N}^b_u \mathbf{u}_b \tag{10}$$

where the shape function arrays $\mathbf{N}^1_\lambda$, $\mathbf{N}^2_\lambda$ and $\mathbf{N}^b_u$ would be dimensioned 2×16, 2×14 and 2×16, respectively, since there are two freedoms per node. Substituting these interpolations into (9) the discrete version results:

$$\begin{aligned} G_{ub}(\boldsymbol{\lambda}^1, \boldsymbol{\lambda}^2, \delta\mathbf{u}_b) &= [(\boldsymbol{\lambda}^1)^{\mathrm{T}} \mathbf{C}_{1b} + (\boldsymbol{\lambda}^2)^{\mathrm{T}} \mathbf{C}_{2b}]\delta\mathbf{u}_b = 0 \\ \mathbf{C}_{kb} &= \int_{\partial\Omega^k_b} (\mathbf{N}^k_\lambda)^{\mathrm{T}} \mathbf{N}^b_u\, \mathrm{d}S, \quad k = 1, 2 \end{aligned} \tag{11}$$

in which $\mathbf{C}_{kb}$ are connection matrices.

The three factors that influence the interface discretization are: (i) interpolation of the localized Lagrange multipliers $\boldsymbol{\lambda}^1$ and $\boldsymbol{\lambda}^2$, (ii) interpolation of the frame displacement $\mathbf{u}_b$, and (iii) preservation of constant stress states when subdomains are connected. The last one is known as the interface patch test. These factors are addressed next.

3.1. Interpolation of localized interface forces $\boldsymbol{\lambda}_\ell$

It has been shown in our previous work [12, 13] that discrete localized Lagrange multipliers $\boldsymbol{\lambda}^1$ and $\boldsymbol{\lambda}^2$ in (11) become the physical nodal forces when they are collocated at the nodes of the corresponding subdomain displacements along the partition boundaries. In interpolating the continuum form of the present localized Lagrange multipliers, this property is preserved

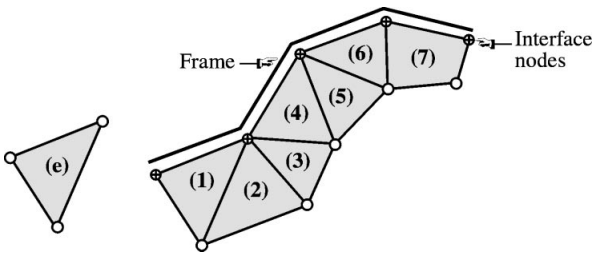

Figure 4. Element-by-element computation of constant stress boundary forces.

by making the multipliers to be point (concentrated) forces at nodes that coincide with the subdomain displacement nodes. This choice is indicated in Figure 3(a) by merging cross and circle symbols. Symbolically, this can be expressed as

$$\lambda_\ell^k = \sum_{j=1}^{N^k} \mathscr{D}(x - x_j)\lambda_\ell^k(x_j), \quad k = 1, 2 \tag{12}$$

where

$$\lambda(x_m)\mathscr{D}(x - x_m) = \begin{cases} \lambda(x_m) & \text{if } x = x_m \\ 0 & \text{otherwise} \end{cases}$$

This choice results in the simplest interface compatibility expression.

3.2. *Computation of constant stress-state interface forces*

As prerequisite to the determination of frame node locations, it is necessary to determine the interface forces associated to a constant stress state σ_c. Those forces are used to obtain the locations of frame nodes that preserve that stress state. For simple elements the calculation of node forces associated to a constant state is straightforward. However, for complex discretizations this task can become burdensome. To this end, we present a simple procedure.

We select a layer of elements along the interface of each partitioned subdomain as illustrated in Figure 4. Consider a typical element (e). From the element library obtain the strain–displacement relation $\mathbf{B}_\varepsilon$ and evaluate this at the element centroid to get $\mathbf{B}_\varepsilon^{(e)}(0)$. The contribution of the element to the constant stress node forces is

$$\mathbf{f}^{(e)} = V[\mathbf{B}_\varepsilon^{(e)}(0)]^{\mathrm{T}}\boldsymbol{\sigma}_c \tag{13}$$

where V denotes the volume, area or length of the element depending on its dimensionality. Once $\mathbf{f}^{(e)}$ is computed for the N_b elements along the interface, the interface forces to be used in the interface patch test for placing frame nodes can be obtained as

$$\boldsymbol{\lambda}_\ell(\sigma_c) = \mathbf{L}^{\mathrm{T}}\mathbf{f}_b, \quad \mathbf{f}_b = \mathbf{A}_b^{\mathrm{T}}\mathbf{f}, \quad \mathbf{f} = [(\mathbf{f}^{(1)})^{\mathrm{T}} \quad (\mathbf{f}^{(2)})^{\mathrm{T}} \quad \dots \quad (\mathbf{f}^{(N_b)})^{\mathrm{T}}]^{\mathrm{T}} \tag{14}$$

where $\mathbf{L}$ is a Boolean extractor of the interface nodal degrees of freedom, and $\mathbf{A}_b$ is the assembly matrix that maps elemental contributions into boundary node forces.

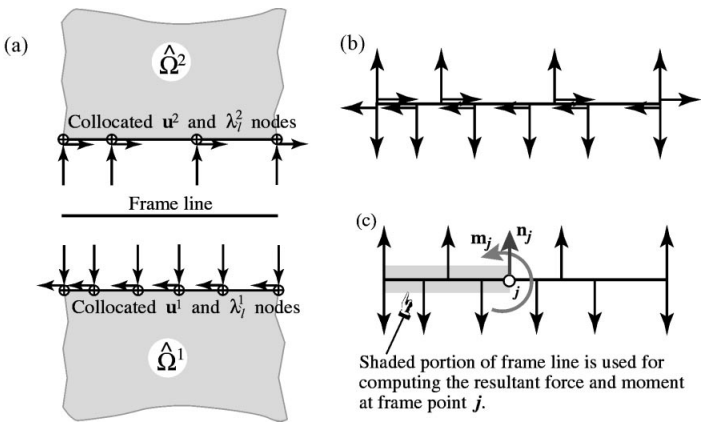

Figure 5. Interface force processing: (a) Interface forces (not scaled, for illustration only); (b) Forces mapped onto frame line; (c) Resultant transverse force n_j and moment m_j acting on frame point j (shear forces not included for clarity).

3.3. *Placement of frame displacement nodes*

Recall that the three-field formulation (2) was extended to a four-field representation (5)–(6) by decomposing subdomain displacements into rigid-body modes (for testing self-equilibrium) and the deformation modes introduced in (4). A similar decomposition of the frame displacement u_{bi} plays a key role in the development of frame-node placement criterion. Thus, the underlying formulation is labeled as a *four-field* variational principle.

Consider the collocated discrete interface forces $\boldsymbol{\lambda}_\ell^1$ and $\boldsymbol{\lambda}_\ell^2$ shown in Figure 5(a) that satisfy a constant stress state over each of the two partitions. When those forces are mapped onto the frame line as depicted in Figure 5(b), the frame, considered as a free body, must be in self-equilibrium. If one restricts the interface forces to those satisfying a constant stress state and if they are in self-equilibrium along the frame line, one concludes that the constant stress state in both subdomains is preserved. This observation will be exploited in the development of a frame-node placement criterion. To this end, consider the resulting force $\mathbf{n}_j$ and moment $\mathbf{m}_j$ and the corresponding frame displacements acting at a frame point $\mathbf{x}_{bj} = (x_j, y_j, z_j)$. This is depicted in Figure 5(c) for the 2D case, in which $z_j = 0$. Define

$$\boldsymbol{\lambda}_{bj} = \left\{ \begin{array}{c} \mathbf{n}_j \\ \mathbf{m}_j \end{array} \right\}, \quad \mathbf{u}_{bj} = \left\{ \begin{array}{c} \mathbf{u}_{xj} \\ \mathbf{u}_{\theta j} \end{array} \right\} \tag{15}$$

If there are M frame nodes along the frame, we must have

$$G_{ub}(\boldsymbol{\lambda}_b, \delta\mathbf{u}_b) = \sum_{j=1} M\boldsymbol{\lambda}_b^{\mathrm{T}}\delta\mathbf{u}_b = \sum_{j=1}^{M} \mathbf{n}_j^{\mathrm{T}}\delta\mathbf{u}_{xj} + \sum_{j=1}^{M} \mathbf{m}_j^{\mathrm{T}}\delta\mathbf{u}_{\theta j} = 0 \tag{16}$$

It should be pointed out that the displacements, $\{\mathbf{u}_{xj},\ j = 1, 2, \ldots, M\}$ and $\{\mathbf{u}_{\theta j},\ j = 1, 2, \ldots, M\}$, are linearly independent if they are not to induce any perturbation in deformation energy in the partitioned subdomains. This requirement will lead to a unique determination of frame nodes.

Figure 6. Rigid-body modes of a 2D frame line: (a) translational; and (b) rotational. Note that their amplitudes are the same everywhere.

The frame motion or displacement $\mathbf{u}_b$ caused by the forces and moments acting along the frame, as illustrated in Figure 5(c), should not trigger changes in deformational energy when the partitioned subdomains are assembled along the frame. In the context of the present four-field variational principle, the frame displacements $\mathbf{u}_b$ consist of the self-equilibrium modes that do not create any perturbation in deformation energy $\mathbf{u}_b^r$ and the deformation modes $\mathbf{u}_b^d$:

$$\mathbf{u}_b = \mathbf{u}_b^r + \mathbf{u}_b^d \tag{17}$$

The only admissible frame displacements that would not cause any deformation on the frame are its self-equilibrium modes, which are in turn the rigid-body modes of the frame. This means that the self-equilibrium translational and rotational nodal displacements are the same for all the frame nodes:

$$\begin{aligned} \mathbf{u}_{x1}^r = \mathbf{u}_{x2}^r = \cdots = \mathbf{u}_{xM}^r = \boldsymbol{\alpha}_x \\ \mathbf{u}_{\theta 1}^r = \mathbf{u}_{\theta 2}^r = \cdots = \mathbf{u}_{\theta M}^r = \boldsymbol{\alpha}_\theta \end{aligned} \tag{18}$$

in which $\boldsymbol{\alpha}_x$ and $\boldsymbol{\alpha}_\theta$ denote the translational and rotational rigid-body amplitudes of the frame, respectively. These two amplitudes are pictured (for the 2D case) in Figure 6.

Substituting (18) into (17) yields

$$G_{ub}(\boldsymbol{\lambda}_b, \delta\mathbf{u}_b^r) = \left[\sum_{j=1}^{M} \mathbf{n}_j^{\mathrm{T}}\right] \delta\boldsymbol{\alpha}_x + \left[\sum_{j=1}^{M} \mathbf{m}_j^{\mathrm{T}}\right] \delta\boldsymbol{\alpha}_\theta = 0 \tag{19}$$

To express the forces and moments at the frame nodes in terms of the localized Lagrange multipliers of each domain mapped onto the frame, we restack $\boldsymbol{\lambda}_\ell^1$ and $\boldsymbol{\lambda}_\ell^2$ so that they are ordered from $\min(\mathbf{x}_b)$ to $\max(\mathbf{x}_b)$. For example, in the case shown in Figure 5(c) $\boldsymbol{\lambda}_\ell$ is restacked from the left to the right:

$$\boldsymbol{\lambda}_\ell = \begin{Bmatrix} \mathbf{n}_\ell \\ \mathbf{m}_\ell \end{Bmatrix} = \mathbf{T}_\ell \begin{Bmatrix} \boldsymbol{\lambda}_\ell^1 \\ \boldsymbol{\lambda}_\ell^2 \end{Bmatrix} \tag{20}$$

For the 2D case illustrated in Figure 5(c) the force n_j and moment m_j are readily obtained from the contributions of the shaded area to the left of j. These resultants may be interpreted as a transverse shear force and bending moment, respectively, if the frame line is viewed as a beam [20].

We now pass to the 3D case illustrated in Figure 7, in which the frame is pictured as planar for visualization simplicity. Using the reordered expression (20) the translational force $\mathbf{n}_k$ and the moment $\mathbf{m}_k$ acting on the frame point k of co-ordinates $\mathbf{x}_k$ can be expressed as

$$\begin{Bmatrix} \mathbf{n}_k \\ \mathbf{m}_k \end{Bmatrix} = \sum_s \begin{bmatrix} \mathbf{I}_s & \mathbf{0} \\ \boldsymbol{\chi}_s^{\mathrm{T}} & \mathbf{I}_s \end{bmatrix} \begin{Bmatrix} \mathbf{n}_{\ell s} \\ \mathbf{m}_{\ell s} \end{Bmatrix}$$

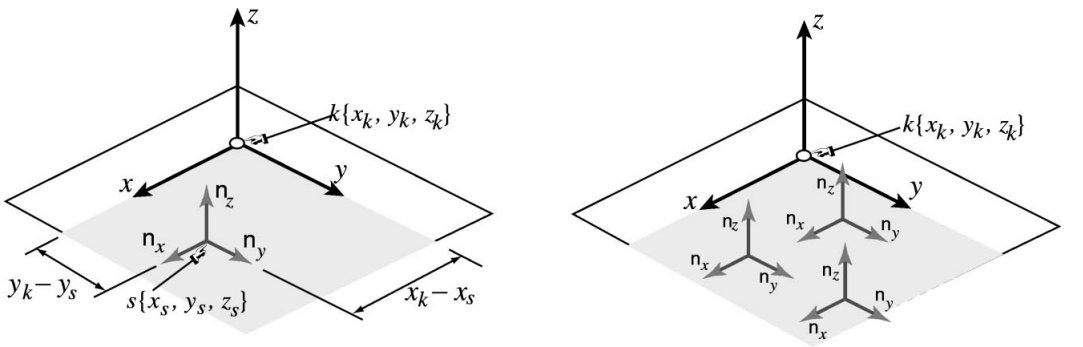

Figure 7. Computation of 3D force resultants at a moving frame point $k(x_k, y_k, z_k)$ produced by interface forces (n_x, n_y, n_z) from a subdomain node s mapped onto the frame and located in the shaded area. Point k sweeps through the frame.

$$\boldsymbol{\chi}_s = \begin{bmatrix} 0 & -(z_k - z_{\ell s}) & (y_k - y_{\ell s}) \\ (z_k - z_{\ell s}) & 0 & -(x_k - x_{\ell s}) \\ -(y_k - y_{\ell s}) & (x_k - x_{\ell s}) & 0 \end{bmatrix} \quad \text{if } (x_k \geqslant x_{\ell s},\ y_k \geqslant y_{\ell s},\ z_k \geqslant z_{\ell s}) \text{ and } \boldsymbol{\chi} = \mathbf{0} \text{ otherwise}$$

$$\mathbf{I}_s = \begin{bmatrix} \mathbf{i}_{xs} & 0 & 0 \\ 0 & \mathbf{i}_{ys} & 0 \\ 0 & 0 & \mathbf{i}_{zs} \end{bmatrix}, \quad \mathbf{i}_{xs} = \begin{cases} 1 & \text{if } x_k - x_{\ell s} \geqslant 0 \\ 0 & \text{if } x_k - x_{\ell s} < 0 \end{cases} \quad \text{and similarly for other expressions} \tag{21}$$

where $(x_{\ell s}, y_{\ell s}, z_{\ell s})$ are the locations where the interface forces are mapped onto the frame.

Substituting $\mathbf{n}_k$ and $\mathbf{m}_k$ from (21) into (19), the variational form of the frame equilibrium condition can be expressed in terms of the constant stress state-satisfying interface forces mapped onto the frame:

$$G_{ub}(\mathbf{n}, \mathbf{m}, \delta\boldsymbol{\alpha}_x, \delta\boldsymbol{\alpha}_\theta) = \left[\sum_{s=1}^{N} \mathbf{n}_{\ell s}^{\mathrm{T}}\right] \delta\boldsymbol{\alpha}_x + [(\mathbf{n}_\ell^{\mathrm{T}} \hat{\boldsymbol{\chi}}_1 + \mathbf{m}_\ell^{\mathrm{T}} \hat{\mathbf{I}}_1) + \cdots + (\mathbf{n}_\ell^{\mathrm{T}} \hat{\boldsymbol{\chi}}_M + \mathbf{m}_\ell^{\mathrm{T}} \hat{\mathbf{I}}_M)]\delta\boldsymbol{\alpha}_\theta = 0$$

$$\hat{\boldsymbol{\chi}}_k^{\mathrm{T}} = \langle \boldsymbol{\chi}(\mathbf{x}_k - \mathbf{x}_{\ell 1})^{\mathrm{T}} \quad \boldsymbol{\chi}(\mathbf{x}_k - \mathbf{x}_{\ell 2})^{\mathrm{T}} \ \cdots \ \boldsymbol{\chi}(\mathbf{x}_k - \mathbf{x}_{\ell N})^{\mathrm{T}} \rangle$$

$$\hat{\mathbf{I}}_k^{\mathrm{T}} = \langle \mathbf{I}(\mathbf{x}_k - \mathbf{x}_{\ell 1})^{\mathrm{T}} \quad \mathbf{I}(\mathbf{x}_k - \mathbf{x}_{\ell 2})^{\mathrm{T}} \ \cdots \ \mathbf{I}(\mathbf{x}_k - \mathbf{x}_{\ell N})^{\mathrm{T}} \rangle \tag{22}$$

$$\mathbf{I}(\mathbf{x}_k - \mathbf{x}_{\ell s}) = \begin{cases} \mathbf{I} & \text{if } \mathbf{x}_k - \mathbf{x}_{\ell s} > \mathbf{0} \\ \mathbf{0} & \text{if } \mathbf{x}_k - \mathbf{x}_{\ell s} \leqslant \mathbf{0} \end{cases}$$

where N is the number of mapped nodes contributing to point k. Since $\boldsymbol{\alpha}_x$ and $\boldsymbol{\alpha}_\theta$ are independent we get the conditions

$$\text{Translational force equilibrium:} \quad \sum_{s=1}^{N} \mathbf{n}_{\ell s}^{\mathrm{T}} = \mathbf{0} \tag{23}$$

$$\text{Moment equilibrium:} \quad [(\mathbf{n}_\ell^{\mathrm{T}} \hat{\boldsymbol{\chi}}_1 + \mathbf{m}_\ell^{\mathrm{T}} \hat{\mathbf{I}}_1) + \cdots + (\mathbf{n}_\ell^{\mathrm{T}} \hat{\boldsymbol{\chi}}_M + \mathbf{m}_\ell^{\mathrm{T}} \hat{\mathbf{I}}_M)] = 0 \tag{24}$$

Note that $\{\boldsymbol{\chi}_k,\ k = 1, 2, \ldots, M\}$ given by (21) is a linear function of the frame co-ordinates. Hence, the feasible locations for the frame nodes are those points which, for the frame co-ordinates $\min\{\mathbf{x}_b\} \leqslant \mathbf{x}_k \leqslant \max\{\mathbf{x}_b\}$, satisfy the moment equilibrium condition (24). A direct search for M nodes is computationally expensive, and is preferable to use the following step-by-step approach. Instead of simultaneously searching for M-points, we incrementally sweep the frame area as illustrated for 2D in Figure 5(c) and for 3D in Figure 7, and identify one frame node at a time. Mathematically, this is equivalent for each term in (24) to vanish:

$$\text{Moment equilibrium at each frame node:} \quad \boxed{\mathbf{n}_\ell^{\mathrm{T}} \hat{\boldsymbol{\chi}}_k + \mathbf{m}_\ell^{\mathrm{T}} \hat{\mathbf{I}}_k = \mathbf{0}, \quad k = 1, 2, \ldots, M} \tag{25}$$

Observe that the translational equilibrium given by (23) remains independent of the frame nodal co-ordinates $\{\mathbf{x}_k,\ k = 1, 2, \ldots, x_M\}$. In fact, for the example two-domain problem shown in Figure 5, (24) becomes

$$\sum_{s=1}^{N^1} \mathbf{n}_{\ell s}^{1\mathrm{T}} + \sum_{s=1}^{N^2} \mathbf{n}_{\ell s}^{2\mathrm{T}} = \mathbf{0} \tag{26}$$

where the superscripts $(1, 2)$ designate partitions 1 and 2, respectively. Moreover, this equation is automatically satisfied if the partitions are in self-equilibrium.

As for the moment equilibrium condition given by (25), let us consider only the case where subdomains are discretized using only the translational degrees of freedom. If so the moment equilibrium condition reduces, for the two-subdomain partition case, to

$$\boxed{\mathbf{n}_\ell^{1\mathrm{T}} \hat{\boldsymbol{\chi}}_k^1 + \mathbf{n}_\ell^{2\mathrm{T}} \hat{\boldsymbol{\chi}}_k^2 = \mathbf{0}, \quad k = 1, 2, \ldots, x_M} \tag{27}$$

A physical interpretation of this criterion is illustrated in Figure 6. The desired frame nodal locations are determined by sweeping over the entire frame area and finding all the frame co-ordinates that satisfy the condition (27). This can be extended to multi-partition cases without any difficulty.

We now summarize the frame node placement criterion:

Frame node locations are determined by the roots of the moment equilibrium condition (25).

Remark 3.1. The placement criterion (27) originally emerged from a study on 2D contact-impact modelling by Rebel *et al.* [21], and may be viewed as a formalization of the contact frame placement algorithm.

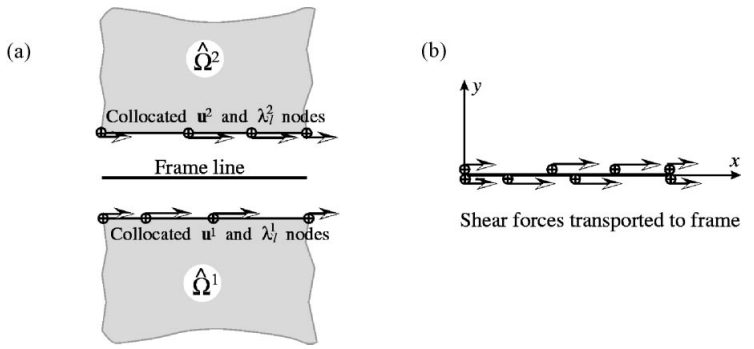

Figure 8. Interface forces for constant shear test.

Remark 3.2. The node placement criterion indicates that piecewise linear interpolation of the frame displacement $\mathbf{u}_b$ is sufficient since the moment equilibrium condition is at most linear in the frame co-ordinates. This suggests two-noded piecewise linear frame elements in 2D, and three-noded triangular or four-noded quadrilateral frame elements in 3D would be sufficient, regardless of the order of the elements being connected.

Remark 3.3. The frame node placement criterion without the rotational degrees of freedom given by (27) can be equivalently expressed in terms of a discrete moment equation for an arbitrary point on the frame, $\mathbf{x} = (x, y, z)$, as follows:

$$\begin{Bmatrix} m_x \\ m_y \\ m_z \end{Bmatrix}_k = \sum_s \begin{bmatrix} 0 & (z_k - z_{\ell s}) & -(y_k - y_{\ell s}) \\ -(z_k - z_{\ell s}) & 0 & (x_k - x_{\ell s}) \\ (y_k - y_{\ell s}) & -(x_k - x_{\ell s}) & 0 \end{bmatrix}^{\mathrm{T}} \begin{Bmatrix} n_x(\mathbf{x}_s) \\ n_y(\mathbf{x}_s) \\ n_z(\mathbf{x}_s) \end{Bmatrix}_\ell = \mathbf{0} \tag{28}$$

with the condition $(x_k \geqslant x_{\ell s}, y_k \geqslant y_{\ell s}, z_k \geqslant z_{\ell s})$.

For a constant shear interface patch test, the tangential interface forces on a 2D frame line are depicted in Figure 8. Then (28) reduces to

$$m_{zk} = \sum_s (y_k - y_{\ell s})\, n_{xs} \tag{29}$$

which is insufficient to define frame node locations. Hence the frame node placement is dictated by the normal load distribution, i.e. $\mathbf{n}_y$ in 2D and $\mathbf{n}_z$ in 3D.

Remark 3.4. In computing the roots of (27) when the frame surface is curved, the translational forces $(\mathbf{n}_x(\mathbf{x}_s), \mathbf{n}_y(\mathbf{x}_s), \mathbf{n}_z(\mathbf{x}_s))_\ell$ that are mapped on the frame surface must be transformed to the local co-ordinates $(\mathbf{x})$ at which (27) is to be evaluated.

3.4. Frame displacement interpolation

When two or more subdomains whose discretization order and mesh sizes are different from one another are brought to interface, two issues arise: possible geometrical gaps along the interfaces and overlap due to different interpolations. The frame displacement $\mathbf{u}_b$ can be viewed

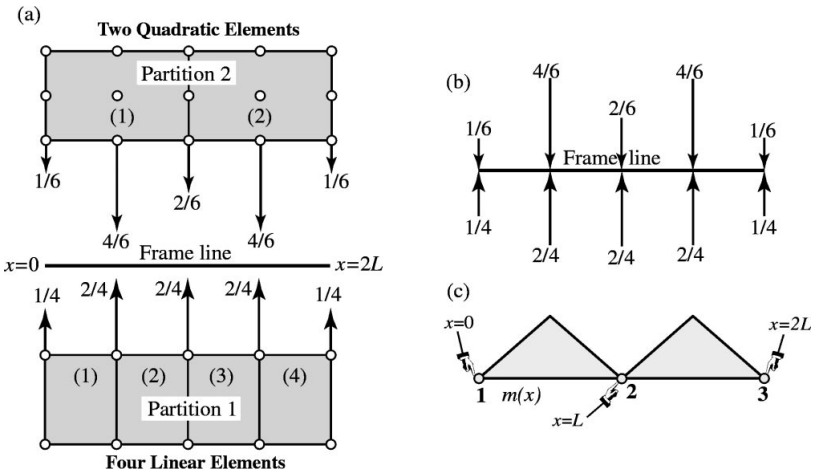

Figure 9. Four linear elements (bottom) connected to two quadratic elements (top): (a) interface forces associated with a constant σ_{yy} stress state (a factor of $L\sigma_{yy}$ has been removed for simplicity); (b) transported frame forces; (c) moment diagram showing candidate frame nodes at zero moment points.

as a mollifier of gaps and overlaps. However, it should be emphasized that $\mathbf{u}_b$ can be interpreted as the global displacement when the partitioned subdomains are assembled together. That is, the deformed co-ordinates along the interface frame are determined by the undeformed co-ordinates at the frame nodes plus the frame displacement $\mathbf{u}_b$. Hence, the deformed coordinates along the interface frame may be viewed as the equilibrated co-ordinates of the partitioned subdomains.

A important question is: when the interfacing subdomains employ different orders of element interpolation, is the order of $\mathbf{u}_b$ controlled by that information? To answer this question we examine the example case depicted in Figure 9.

Partition 1 is discretized by four plane stress linear elements and partition 2 by two quadratic elements. The σ_{yy}-constant interface forces $\boldsymbol{\lambda}_p^1$ and $\boldsymbol{\lambda}_p^2$ (with a factor of $2L\sigma_{yy}$ removed) are shown in Figure 9(a) and transported to the frame line as shown in Figure 9(b). The moment diagram $m(x)$ as point $x \equiv x_k$ sweeps the frame is shown in Figure 9(c). This function has three zero-moment roots at $x = 0, L, 2L$, where L is the x-length of the quadratic element. As noted in Remark 3.2, the linear dependence of the frame self-equilibrium equation (27) suggest that the frame displacement $\mathbf{u}_b$ be approximated by two-noded linear approximations:

$$u_b = \begin{cases} (1 - \frac{x}{L})u_{b1} + \frac{x}{L}u_{b2}, & 0 \leqslant x \leqslant L \\ (1 - \frac{x-L}{L})u_{b2} + \frac{x-L}{L}u_{b3}, & L \leqslant x \leqslant 2L \end{cases} \tag{30}$$

Consequently, the frame displacement is discretized with less nodes than the number of nodes on either side of the interface. To examine the impact of the frame interpolation (30), let us discretize the interface constraint functional (3)

$$\pi_u = \int_{\partial\Omega_b^1 \cup \partial\Omega_u^1} \lambda_\ell^1 (u^1 - u_b)\, \mathrm{d}S + \int_{\partial\Omega_b^2 \cup \partial\Omega_u^2} \lambda_\ell^2 (u^2 - u_b)\, \mathrm{d}S \tag{3'}$$

Since $\boldsymbol{\lambda}^1$ and $\boldsymbol{\lambda}^2$ are collocated with the interface displacement nodes, we obtain

$$\int_{\partial\Omega_b^1\cup\partial\Omega_u^1}\lambda_\ell^1 u^1\,\mathrm{d}S=(\boldsymbol{\lambda}^1)^{\mathrm{T}}\mathbf{u}^1,\quad \int_{\partial\Omega_b^2\cup\partial\Omega_u^2}\lambda_\ell^2 u^2\,\mathrm{d}S=(\boldsymbol{\lambda}^2)^{\mathrm{T}}\mathbf{u}^2 \tag{31}$$

where $\boldsymbol{\lambda}^1$, $\boldsymbol{\lambda}^2$, $\mathbf{u}^1$ and $\mathbf{u}^2$ are given by

$$\boldsymbol{\lambda}^1=\begin{Bmatrix}\lambda_{(1)}\\ \lambda_{(2)}\\ \lambda_{(3)}\\ \lambda_{(4)}\\ \lambda_{(5)}\end{Bmatrix}^1,\quad \boldsymbol{\lambda}^2=\begin{Bmatrix}\lambda_{(1)}\\ \lambda_{(2)}\\ \lambda_{(3)}\\ \lambda_{(4)}\\ \lambda_{(5)}\end{Bmatrix}^2,\quad \mathbf{u}^1=\begin{Bmatrix}u_{(1)}\\ u_{(2)}\\ u_{(3)}\\ u_{(4)}\\ u_{(5)}\end{Bmatrix}^1,\quad \mathbf{u}^2=\begin{Bmatrix}u_{(1)}\\ u_{(2)}\\ u_{(3)}\\ u_{(4)}\\ u_{(5)}\end{Bmatrix}^2 \tag{32}$$

Using the Dirac's delta function representation of the multipliers reduces the interface integrals to point collocation

$$\begin{aligned}&\int_{\partial\Omega_b^1\cup\partial\Omega_u^1}\lambda_\ell^1 u_b\,\mathrm{d}S=(\boldsymbol{\lambda}^1)^{\mathrm{T}}\mathbf{L}_{b1}\mathbf{u}_b,\quad \mathbf{L}_{b1}=\begin{bmatrix}1&0&0\\ \frac{1}{2}&\frac{1}{2}&0\\ 0&1&0\\ 0&\frac{1}{2}&\frac{1}{2}\\ 0&0&1\end{bmatrix},\quad \mathbf{u}_b=\begin{Bmatrix}u_{b1}\\ u_{b2}\\ u_{b3}\end{Bmatrix}\\ &\int_{\partial\Omega_b^2\cup\partial\Omega_u^2}\lambda_\ell^2 u_b\,\mathrm{d}S=(\boldsymbol{\lambda}^2)^{\mathrm{T}}\mathbf{L}_{b2}\mathbf{u}_b,\quad \mathbf{L}_{b2}=\begin{bmatrix}1&0&0\\ \frac{1}{2}&\frac{1}{2}&0\\ 0&1&0\\ 0&\frac{1}{2}&\frac{1}{2}\\ 0&0&1\end{bmatrix}\end{aligned} \tag{33}$$

Substituting (31) and (33) into (3′) we obtain

$$\delta\pi_u=\begin{Bmatrix}\delta\boldsymbol{\lambda}^1\\ \delta\boldsymbol{\lambda}^2\end{Bmatrix}^{\mathrm{T}}\left\{\begin{Bmatrix}\mathbf{u}^1\\ \mathbf{u}^2\end{Bmatrix}-\begin{bmatrix}\mathbf{L}_{b1}\\ \mathbf{L}_{b2}\end{bmatrix}\mathbf{u}_b\right\}+\begin{Bmatrix}\boldsymbol{\lambda}^1\\ \boldsymbol{\lambda}^2\end{Bmatrix}^{\mathrm{T}}\left\{\begin{Bmatrix}\delta\mathbf{u}^1\\ \delta\mathbf{u}^2\end{Bmatrix}-\begin{bmatrix}\mathbf{L}_{b1}\\ \mathbf{L}_{b2}\end{bmatrix}\delta\mathbf{u}_b\right\}=0 \tag{34}$$

whence the discrete connection equations follow as

$$\begin{Bmatrix}\mathbf{u}^1\\ \mathbf{u}^2\end{Bmatrix}-\begin{bmatrix}\mathbf{L}_{b1}\\ \mathbf{L}_{b2}\end{bmatrix}\mathbf{u}_b=0,\quad [\mathbf{L}_{b1}^{\mathrm{T}}\quad \mathbf{L}_{b2}^{\mathrm{T}}]\begin{Bmatrix}\boldsymbol{\lambda}^1\\ \boldsymbol{\lambda}^2\end{Bmatrix}=0 \tag{35}$$

In the foregoing, the terms associated with the variation of the subdomain displacements $\delta\mathbf{u}^1$ and $\delta\mathbf{u}^2$ do not vanish; they are combined with the equilibrium equations for completely free subdomains. It should be noted that, although the u_b interpolation does not explicitly connect $u_{(2)}^1$ to $u_{(2)}^2$, and $u_{(4)}^1$ to $u_{(4)}^2$, once the solution of $\mathbf{u}_b$ is obtained, the second equation of the

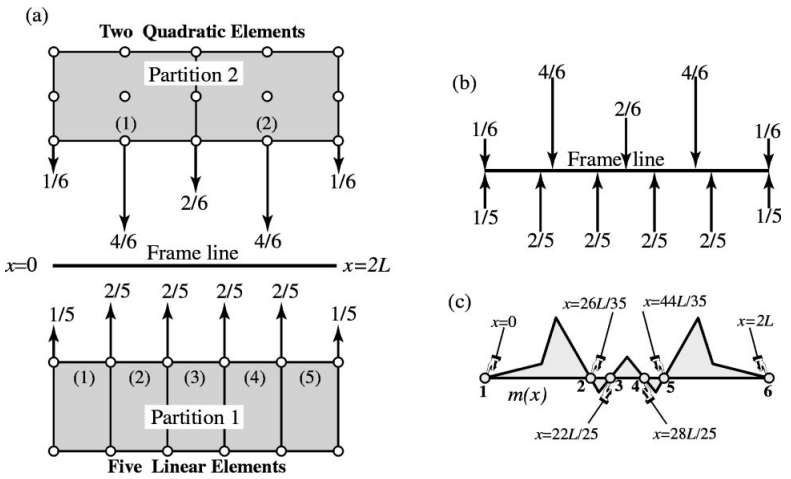

Figure 10. Five linear elements (bottom) connected to two quadratic elements (top): (a) interface forces associated to uniform σ_{yy} stress state (a factor of $L\sigma_{yy}$ has been removed for simplicity); (b) transported frame forces; (c) moment diagram showing candidate frame nodes at zero moment points.

set (35) yields

$$\left\{ \begin{array}{l} u^1_{(2)} = \frac{1}{2}(u_{b1} + u_{b2}) \\ u^2_{(2)} = \frac{1}{2}(u_{b1} + u_{b2}) \end{array} \right\} \;\Rightarrow\; u^1_{(2)} = u^2_{(2)} \quad \text{and similarly } u^1_{(4)} = u^2_{(4)} \tag{36}$$

Remark 3.5. In this particular example *both nodes and degrees of freedom match* yet the interface is nonmatching. It would be a serious mistake to introduce two additional frame nodes at $x = \frac{1}{2}L$ and $x = \frac{3}{2}L$ (as it would seem natural to practitioners of master–slave methods) since the interface patch test for constant σ_{yy} would be violated.

4. ILLUSTRATIVE EXAMPLES

4.1. Linear–quadratic non-matching nodes

This example is depicted in Figure 10. Partition 1 consists of two quadratic plane stress elements whereas partition 2 consists of five linear plane stress elements. As shown in Figure 10, the nodes do not match. In order to construct the frame nodes, a uniform σ_{yy} stress state is imposed on both partitions. The corresponding interface forces (with a factor $L\sigma_{yy}$ removed) are shown in Figure 10(a). They are transported to the frame line as shown in Figure 10(b). The six roots of the moment diagram shown in Figure 10(c) and marked with ○, are at

$$x_b = \{0, 13/35, 11/25, 14/25, 22/35, 1\}2L \tag{37}$$

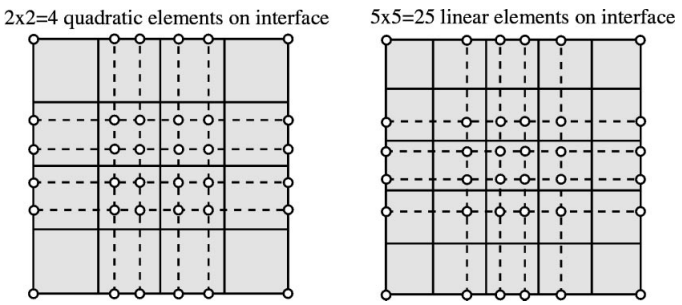

Figure 11. Extension of configuration of Figure 10 to three dimensions. The figures depict the two sides of the interface. Dashed lines and circles identify frame meshes and frame nodes, respectively.

These are selected as frame node locations, and the frame displacements are interpolated linearly between them. We find that the frame-to-subdomain linking matrices $\mathbf{L}_{b1}$ and $\mathbf{L}_{b2}$ are

$$\mathbf{L}_{b1} = \begin{bmatrix} 1 & 0 & 0 & 0 & 0 & 0 \\ 6/13 & 7/13 & 0 & 0 & 0 & 0 \\ 0 & 7/12 & 5/12 & 0 & 0 & 0 \\ 0 & 0 & 0 & 5/12 & 7/12 & 0 \\ 0 & 0 & 0 & 0 & 7/13 & 6/13 \\ 0 & 0 & 0 & 0 & 0 & 1 \end{bmatrix}$$

$$\mathbf{L}_{b2} = \begin{bmatrix} 1 & 0 & 0 & 0 & 0 & 0 \\ 17/52 & 35/52 & 0 & 0 & 0 & 0 \\ 0 & 0 & 1/2 & 1/2 & 0 & 0 \\ 0 & 0 & 0 & 0 & 35/52 & 17/52 \\ 0 & 0 & 0 & 0 & 0 & 1 \end{bmatrix} \tag{38}$$

The localized interface compatibility condition is given by the second of (35). It should be emphasized that the frame-to-subdomain operator $\mathbf{L}_{bi}$ is uniquely determined once the frame nodes are found. On the other hand, the classical Lagrange multiplier method which interfaces the two partitions directly, does not lead to a unique connection matrix, as discussed later.

The findings for the 2D case are readily extended to a 3D configuration if the interface geometry is rectangular and planar. This is illustrated in Figure 11, where it is assumed that a solid mesh with $2 \times 2 = 4$ quadratic elements is interfaced to another solid mesh with $5 \times 5 = 25$ linear elements. The frame nodes are obtained directly from a product application of the solution of Figure 10(c).

4.2. Linear–quadratic interfacing by master–slave approach

Let us reconsider the problem of Figure 10 using a master–slave approach. If partition 1 is chosen as the master interface, the following interface condition is obtained:

$$\mathbf{u}^2 - \mathbf{L}_{21}\mathbf{u}^1 = 0, \quad \mathbf{L}_{21} = \begin{bmatrix} 1 & 0 & 0 & 0 & 0 & 0 \\ 0 & 3/4 & 1/4 & 0 & 0 & 0 \\ 0 & 0 & 1/2 & 1/2 & 0 & 0 \\ 0 & 0 & 0 & 1/4 & 3/4 & 0 \\ 0 & 0 & 0 & 0 & 0 & 1 \end{bmatrix} \tag{39}$$

On the other hand, if partition 2 is taken as master, the interface condition is

$$\mathbf{u}^1 - \mathbf{L}_{12}\mathbf{u}^2 = 0, \quad \mathbf{L}_{12} = \frac{1}{25}\begin{bmatrix} 25 & 0 & 0 & 0 & 0 \\ 3 & 24 & -2 & 0 & 0 \\ -3 & 16 & 12 & 0 & 0 \\ 0 & 0 & 12 & 16 & -3 \\ 0 & 0 & -2 & 24 & 3 \\ 0 & 0 & 0 & 0 & 25 \end{bmatrix} \tag{40}$$

Since these matrices are not square, there exists no unique way of transforming one relation to the other. This means that the master–slave approach does not lead to a unique result.

In terms of the classical Lagrange multiplier method, the use of either (39) or (40) leads to a master–slave interface operator as shown by $\mathbf{L}_{21}$ and $\mathbf{L}_{12}$. Since there is no guarantee that either of them will satisfy the interface patch test, one may pursue instead a least-squares approach by solving the following equation:

$$\begin{bmatrix} \mathbf{I}^2 \\ \mathbf{L}_{12} \end{bmatrix}\mathbf{u}^2 - \begin{bmatrix} \mathbf{L}_{21} \\ \mathbf{I}^1 \end{bmatrix}\mathbf{u}^1 = 0 \Rightarrow \mathbf{u}^2 - \mathbf{L}_{21}^{\mathrm{LS}}\mathbf{u}^1 = 0, \quad \mathbf{L}_{21}^{\mathrm{LS}} = [\mathbf{I}^2 + \mathbf{L}_{12}^{\mathrm{T}}\mathbf{L}_{12}]^{-1}[\mathbf{L}_{21} + \mathbf{L}_{12}^{\mathrm{T}}] \tag{41}$$

This is a least-squares master–slave interface condition if partition 1 is chosen as the master interface. If partition 2 is chosen as master, the resulting least-squares constraint condition would be different.

One can deduce a least-squares master–slave constraint from the localized interface condition (35) as follows. First, we express it as

$$\begin{Bmatrix} \mathbf{u}^1 \\ \mathbf{u}^2 \end{Bmatrix} - \mathbf{L}_b\mathbf{u}_b = \mathbf{0}, \quad \mathbf{L}_b = \begin{bmatrix} \mathbf{L}_{b1} \\ \mathbf{L}_{b2} \end{bmatrix} \tag{42}$$

Second, a null-space $\mathbf{N}_b$ of $\mathbf{L}_b$ defined by

$$\mathbf{N}_b = \mathrm{null}(\mathbf{L}_b) \quad \text{such that } \mathbf{N}_b\mathbf{L}_b = \mathbf{0} \tag{43}$$

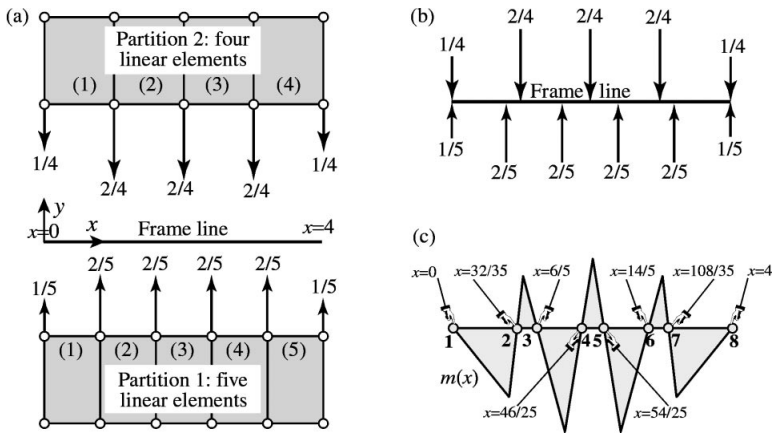

Figure 12. Interfacing four 2D linear elements (top) to five linear elements (bottom): (a) interface forces associated with a constant $\sigma_{yy} = \frac{1}{2}$ stress state; (b) forces transported to frame line; (c) roots of moment diagram $m(x)$.

is extracted. Third, $\mathbf{u}_b$ is eliminated on pre-multiplying (42) with $\mathbf{N}_b$ to obtain

$$\mathbf{N}_b \begin{Bmatrix} \mathbf{u}^1 \\ \mathbf{u}^2 \end{Bmatrix} = \mathbf{0} \tag{44}$$

Remark 4.1. Matrix $\mathbf{N}_b$ is generally dense, hindering sparsity of the coupled system matrices. This technique can be viewed as an approximation to the classical Lagrange multiplier method applied with smooth global functions. Nevertheless, the master–slave operator obtained from the present localized algorithm $\mathbf{N}_b$ should satisfy the interface patch test whereas there is no definite theory as to whether $\mathbf{L}_{21}^{LS}$ or $\mathbf{L}_{12}^{LS}$ would pass the test.

4.3. Linear–linear non-matching localized interfaces

Consider next the case shown in Figure 12, where partitions 1 and 2 are discretized with 4 and 5 linear elements, respectively, across the interface of length $L = 4$. The forces corresponding from a uniform $\sigma_{yy} = \frac{1}{2}$ stress state are shown in Figure 12(a) and transported to the frame line in Figure 12(b). The moment diagram $m(x)$ is depicted in Figure 12(c). The zero moment condition gives the eight roots

$$\mathbf{x}_b = \{0, 32/35, 6/5, 46/25, 54/25, 14/5, 108/35, 4\} \tag{45}$$

as candidates for frame node locations. The mesh of partition 1 is slightly finer than that of partition 2, with six interface nodes. The maximum number of frame nodes is eight, which exceeds that of partition 1. However, this does not cause numerical problems since the resulting localized compatibility matrix $\mathbf{L}_b$ has full column rank and its row size is at least the same or larger than its column size. In fact, using the 8 roots one obtains through

collocation the following interface compatibility relation:

$$\mathbf{u}-\mathbf{L}_b\mathbf{u}_b=\mathbf{0},\quad \mathbf{u}=\begin{Bmatrix}\mathbf{u}^1\\ \mathbf{u}^2\end{Bmatrix},\quad \mathbf{L}_b=\begin{bmatrix} 1 & 0 & 0 & 0 & 0 & 0 & 0 & 0\\ 1/8 & 7/8 & 0 & 0 & 0 & 0 & 0 & 0\\ 0 & 0 & 3/8 & 5/8 & 0 & 0 & 0 & 0\\ 0 & 0 & 0 & 0 & 5/8 & 3/8 & 0 & 0\\ 0 & 0 & 0 & 0 & 0 & 0 & 7/8 & 1/8\\ 0 & 0 & 0 & 0 & 0 & 0 & 0 & 1\\ 1 & 0 & 0 & 0 & 0 & 0 & 0 & 0\\ 0 & 7/10 & 3/10 & 0 & 0 & 0 & 0 & 0\\ 0 & 0 & 0 & 1/2 & 1/2 & 0 & 0 & 0\\ 0 & 0 & 0 & 0 & 0 & 3/10 & 7/10 & 0\\ 0 & 0 & 0 & 0 & 0 & 0 & 0 & 1 \end{bmatrix} \tag{46}$$

If all eight roots are used, the size of some frame elements may be considered too small, e.g. the second and the sixth frame elements in Figure 12(c). If this is a concern some of the frame nodes may be omitted. For example, if frame nodes 2 and 7 are discarded the retained node positions are

$$\mathbf{x}_b=\{0,6/5,46/25,54/25,14/5,4\} \tag{47}$$

which yields the six-column frame-to-interface matrix

$$\mathbf{L}_b=\begin{bmatrix} 1 & 0 & 0 & 0 & 0 & 0\\ 1/3 & 2/3 & 0 & 0 & 0 & 0\\ 0 & 3/8 & 5/8 & 0 & 0 & 0\\ 0 & 0 & 0 & 5/8 & 3/8 & 0\\ 0 & 0 & 0 & 0 & 2/3 & 1/3\\ 0 & 0 & 0 & 0 & 0 & 1\\ 1 & 0 & 0 & 0 & 0 & 0\\ 1/6 & 5/6 & 0 & 0 & 0 & 0\\ 0 & 0 & 1/2 & 1/2 & 0 & 0\\ 0 & 0 & 0 & 0 & 5/6 & 1/6\\ 0 & 0 & 0 & 0 & 0 & 1 \end{bmatrix} \tag{48}$$

The extension of this 2D configuration to a regular 3D meshes is illustrated in Figure 13. Here frame meshes and frame node location are constructed from (47). A master–slave approach would not lead to an equivalent form of the present results.

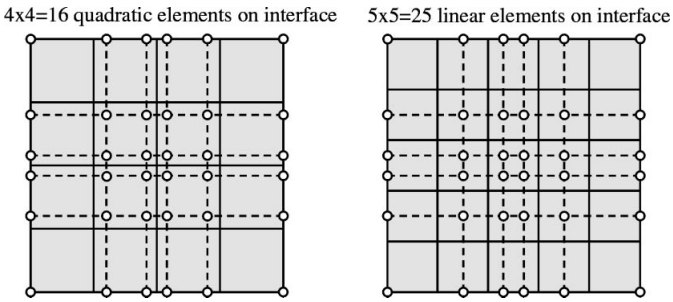

Figure 13. Extension of the configuration of Figure 12 to three dimensions. The figures depict the two sides of the interface. Dashed lines and circles identify frame meshes and frame nodes, respectively.

5. SYSTEM EQUATIONS

5.1. Partitioned dynamic system equations

As stated in (2) and (3), the discrete form of the energy functional for a *completely free* undamped partitioned domain Π^m_{PE} (3′) can be expressed as [12, 13]

$$\delta\Pi^m_{\mathrm{PE}}(\mathbf{u}^m) = (\delta\mathbf{u}^m)^{\mathrm{T}}\,[\mathbf{K}^m\mathbf{u}^m - (\mathbf{f}^m - \mathbf{M}^m\ddot{\mathbf{u}}^m)] \tag{49}$$

where $\mathbf{u}^m$ is the displacement for subdomain m, $\mathbf{K}^m$ is the stiffness matrix, $\mathbf{M}^m$ is the mass matrix, and $\mathbf{f}^m$ is the sum of the applied force and prescribed boundary tractions.

For notational simplicity, we use $\mathbf{u}^m$ as the total degrees of freedom for subdomain m. The subdomain interface degrees of freedom at subdomain m will be expressed as

$$\mathbf{u}^m_{interface} = (\mathbf{B}^m)^{\mathrm{T}}\mathbf{u}^m \tag{50}$$

where $\mathbf{B}^m$ is a Boolean matrix that extracts only the subdomain interface nodal degrees of freedom. The discrete energy functional for the *completely free* total partitioned domains can thus be written as

$$\delta\Pi_{\mathrm{PE}}(\mathbf{u}) = \delta\mathbf{u}^{\mathrm{T}}[\mathbf{K}\mathbf{u} - (\mathbf{f} - \mathbf{M}\ddot{\mathbf{u}})]$$

$$\mathbf{K} = \begin{bmatrix} \mathbf{K}^1 & 0 & 0 & \dots & 0 \\ 0 & \mathbf{K}^2 & 0 & \dots & 0 \\ . & . & . & \dots & . \\ 0 & 0 & 0 & \dots & \mathbf{K}^{N_s} \end{bmatrix}, \quad \mathbf{M} = \begin{bmatrix} \mathbf{M}^1 & 0 & 0 & \dots & 0 \\ 0 & \mathbf{M}^2 & 0 & \dots & 0 \\ . & . & . & \dots & . \\ 0 & 0 & 0 & \dots & \mathbf{M}^{N_s} \end{bmatrix}$$

$$\mathbf{u} = \begin{Bmatrix} \mathbf{u}^1 \\ \mathbf{u}^2 \\ . \\ \mathbf{u}^{N_s} \end{Bmatrix}, \quad \mathbf{f} = \begin{Bmatrix} \mathbf{f}^1 \\ \mathbf{f}^2 \\ . \\ \mathbf{f}^{N_s} \end{Bmatrix} \tag{51}$$

in which N_s is the total number of partitions (substructures). The variation of the localized interface functional π_u can be written as

$$\delta\pi_u(\mathbf{u},\boldsymbol{\lambda}_\ell,\mathbf{u}_b) = \delta\boldsymbol{\lambda}_\ell^{\mathrm{T}}\{\mathbf{B}^{\mathrm{T}}\mathbf{u}-\mathbf{L}_b\mathbf{u}_b\}+\boldsymbol{\lambda}_\ell^{\mathrm{T}}\{\mathbf{B}^{\mathrm{T}}\delta\mathbf{u}-\mathbf{L}_b\delta\mathbf{u}_b\}=0$$
$$\mathbf{B}=\begin{bmatrix}\mathbf{B}^1 & 0 & 0 & \dots & 0\\ 0 & \mathbf{B}^2 & 0 & \dots & 0\\ . & . & . & \dots & .\\ 0 & 0 & 0 & \dots & \mathbf{B}^{N_s}\end{bmatrix},\quad \boldsymbol{\lambda}_\ell=\begin{Bmatrix}\boldsymbol{\lambda}^1\\ \boldsymbol{\lambda}^2\\ .\\ \boldsymbol{\lambda}^{N_s}\end{Bmatrix} \tag{52}$$

where $\mathbf{L}_b$ is the collection of the frame-to-interface matrices as determined by following the frame nodal placement criterion for all the frames of the partitioned subdomains.

The discrete form of the three-field functional $\delta\Pi_{\mathrm{PEM2}}$ (2) for the total partitioned systems is thus obtained by the sum of (51) and (52):

$$\delta\Pi_{\mathrm{PEM2}}(\mathbf{u},\boldsymbol{\lambda}_\ell,\mathbf{u}_b) = \delta\Pi_{\mathrm{PE}}(\mathbf{u})+\delta\pi_u(\mathbf{u},\boldsymbol{\lambda}_\ell,\mathbf{u}_b)$$
$$=\begin{Bmatrix}\delta\mathbf{u}\\ \delta\boldsymbol{\lambda}_\ell\\ \delta\mathbf{u}_b\end{Bmatrix}^{\mathrm{T}}\left(\begin{bmatrix}\mathbf{K}-\mathbf{M}\dfrac{\mathrm{d}^2}{\mathrm{d}t^2} & \mathbf{B} & \mathbf{0}\\ \mathbf{B}^{\mathrm{T}} & \mathbf{0} & -\mathbf{L}_b\\ \mathbf{0} & -\mathbf{L}_b^{\mathrm{T}} & \mathbf{0}\end{bmatrix}\begin{Bmatrix}\mathbf{u}\\ \boldsymbol{\lambda}_\ell\\ \mathbf{u}_b\end{Bmatrix}-\begin{Bmatrix}\mathbf{f}\\ 0\\ 0\end{Bmatrix}\right) \tag{53}$$

This is valid for matching as well as non-matching interface meshes. The preceding three-field discrete variational equation can be expanded into a four-field equation by introducing the discrete counterpart of (4):

$$\mathbf{u}=\mathbf{R}\boldsymbol{\alpha}+\boldsymbol{\Phi}\mathbf{q} \tag{54}$$

with orthogonality conditions $\mathbf{R}^{\mathrm{T}}\mathbf{M}\boldsymbol{\Phi}=\mathbf{0}$ and $\mathbf{R}^{\mathrm{T}}\mathbf{K}=\mathbf{0}$. Substituting into the three-field equation (53) yields

$$\delta\Pi_{\mathrm{PEM2}}(\mathbf{q},\boldsymbol{\alpha},\boldsymbol{\lambda}_\ell,\mathbf{u}_b)$$
$$=\begin{Bmatrix}\delta\mathbf{q}\\ \delta\boldsymbol{\alpha}\\ \delta\boldsymbol{\lambda}_\ell\\ \delta\mathbf{u}_b\end{Bmatrix}^{\mathrm{T}}\left(\begin{bmatrix}\mathbf{K}_{\phi\phi}-\mathbf{M}_{\phi\phi}\dfrac{\mathrm{d}^2}{\mathrm{d}t^2} & \mathbf{0} & \boldsymbol{\Phi}_b^{\mathrm{T}} & \mathbf{0}\\ \mathbf{0} & -\mathbf{M}_{\alpha\alpha}\dfrac{\mathrm{d}^2}{\mathrm{d}t^2} & \mathbf{R}_b^{\mathrm{T}} & \mathbf{0}\\ \boldsymbol{\Phi}_b & \mathbf{R}_b & \mathbf{0} & -\mathbf{L}_b\\ \mathbf{0} & \mathbf{0} & -\mathbf{L}_b^{\mathrm{T}} & \mathbf{0}\end{bmatrix}\begin{Bmatrix}\mathbf{q}\\ \boldsymbol{\alpha}\\ \boldsymbol{\lambda}_\ell\\ \mathbf{u}_b\end{Bmatrix}-\begin{Bmatrix}\boldsymbol{\Phi}^{\mathrm{T}}\mathbf{f}\\ \mathbf{R}^{\mathrm{T}}\mathbf{f}\\ 0\\ 0\end{Bmatrix}\right) \tag{55}$$

$$\mathbf{K}_{\phi\phi}=\boldsymbol{\Phi}^{\mathrm{T}}\mathbf{K}\boldsymbol{\Phi},\quad \mathbf{M}_{\phi\phi}=\boldsymbol{\Phi}^{\mathrm{T}}\mathbf{M}\boldsymbol{\Phi},\quad \mathbf{M}_{\alpha\alpha}=\mathbf{R}^{\mathrm{T}}\mathbf{M}\mathbf{R},\quad \boldsymbol{\Phi}_b^{\mathrm{T}}=\boldsymbol{\Phi}^{\mathrm{T}}\mathbf{B},\quad \mathbf{R}_b^{\mathrm{T}}=\mathbf{R}^{\mathrm{T}}\mathbf{B}$$

For static problems the inertial terms are dropped and $\mathbf{K}_{\phi\phi}$ may be kept as $\mathbf{K}$ while using $\mathbf{d}=\boldsymbol{\Phi}\mathbf{q}$. Thus, the stationarity of (55) gives the following partitioned equations:

$$\begin{bmatrix}\mathbf{K} & \mathbf{0} & \mathbf{B} & \mathbf{0}\\ \mathbf{0} & \mathbf{0} & \mathbf{R}_b^{\mathrm{T}} & \mathbf{0}\\ \mathbf{B}^{\mathrm{T}} & \mathbf{R}_b & \mathbf{0} & -\mathbf{L}_b\\ \mathbf{0} & \mathbf{0} & -\mathbf{L}_b^{\mathrm{T}} & \mathbf{0}\end{bmatrix}\begin{bmatrix}\mathbf{d}\\ \boldsymbol{\alpha}\\ \boldsymbol{\lambda}_\ell\\ \mathbf{u}_b\end{bmatrix}=\begin{bmatrix}\mathbf{f}\\ \mathbf{R}^{\mathrm{T}}\mathbf{f}\\ \mathbf{0}\\ \mathbf{0}\end{bmatrix} \tag{56}$$

The nodal deformation vector $\mathbf{q}$ can be obtained from the first matrix equation as $\mathbf{d}=\mathbf{F}(\mathbf{f}-\mathbf{B}\boldsymbol{\lambda}_\ell)$, where $\mathbf{F}=\mathbf{K}^+$ is the free–free flexibility, or Moore–Penrose generalized inverse of $\mathbf{K}$. This matrix can be efficiently obtained, subdomain by subdomain, as described by Felippa *et al.* [22]. Substituting this into the third row of (56) gives

$$\mathbf{B}^{\mathrm{T}}\mathbf{F}\mathbf{B}\boldsymbol{\lambda}_\ell - \mathbf{R}_b\boldsymbol{\alpha} + \mathbf{L}_b\mathbf{u}_b = \mathbf{B}^{\mathrm{T}}\mathbf{F}\mathbf{f}, \quad \mathbf{F}_b = \mathbf{B}^{\mathrm{T}}\mathbf{F}\mathbf{B} \tag{57}$$

Combining the second and fourth rows with that equation, one arrives at the following partitioned flexibility equation:

$$\begin{bmatrix} \mathbf{F}_b & -\mathbf{R}_b & \mathbf{L}_b \\ -\mathbf{R}_b^{\mathrm{T}} & \mathbf{0} & \mathbf{0} \\ \mathbf{L}_b^{\mathrm{T}} & \mathbf{0} & \mathbf{0} \end{bmatrix} \begin{bmatrix} \boldsymbol{\lambda}_\ell \\ \boldsymbol{\alpha} \\ \mathbf{u}_b \end{bmatrix} = \begin{bmatrix} \mathbf{h}_b \\ -\mathbf{f}_\alpha \\ \mathbf{0} \end{bmatrix}, \quad \mathbf{h}_b = \mathbf{B}^{\mathrm{T}}\mathbf{F}\mathbf{f}, \quad \mathbf{f}_\alpha = \mathbf{R}^{\mathrm{T}}\mathbf{f} \tag{58}$$

The partitioned flexibility equation (58) and its dynamic counterpart have been applied to parallel computations [23–26], damage detection [27], system identification [28], structural joint identification [29], and distributed vibration control problems [30].

Remark 5.1. The construction of the frame-to-partition interface nodal relation matrix $\mathbf{L}_b$ can be implemented as a stand-alone software module because the construction of the interface operators does not require detailed knowledge about the type of element being interfaced. Hence, the modelling and analysis software for each partition is not seriously affected.

Remark 5.2. As shown in Sections 3 and 4, the construction of the frame-to-partition interface nodal relation matrix $\mathbf{L}_b$ does not involve any global spatial interface integration. They are simply the weighting factors for the locally interpolated shape functions of the frame displacement $\mathbf{u}_b$.

Remark 5.3. The incorporation of the present interfacing method is not tied up to any special solution algorithm. It can be implemented in a direct solver, or as a parallel iterative algorithm [24, 26].

5.2. *Analysis of solid with non-matching interface*

The present interface algorithm is demonstrated in the problem shown in Figure 14. The complete system models a solid bar of length 4 with a 1×1 square cross-section. The FEM model is partitioned into four subdomains along z, with one element in the longitudinal direction. The lower two subdomains have a $5\times$ regular mesh in their cross-section whereas the top two domains have a $4\times$ regular mesh. The elastic modulus and Poisson's ratio are $E=2600$ psi and $v=0.3$, respectively. The boundary conditions set the z displacement of the bottom subdomain equal to zero at the bottom while lateral expansion can occur freely to ensure a constant stress state. The top domain is loaded by a prescribed displacement of 0.4 downward at its top face. As a result the z axial strain will be -0.1 which gives a uniform $\sigma_{zz}=-260$ psi, which is also the Von Mises stress for this case. The final z position of the frame between subdomains 2 and 3 becomes 1.8, which is the value corresponding to the green color of the frame.

There are three interface frames that lie between subdomains 1 and 2, subdomains 2 and 3, and subdomains 3 and 4. Since subdomains 1 and 2 are both discretized by a regular (5×5)

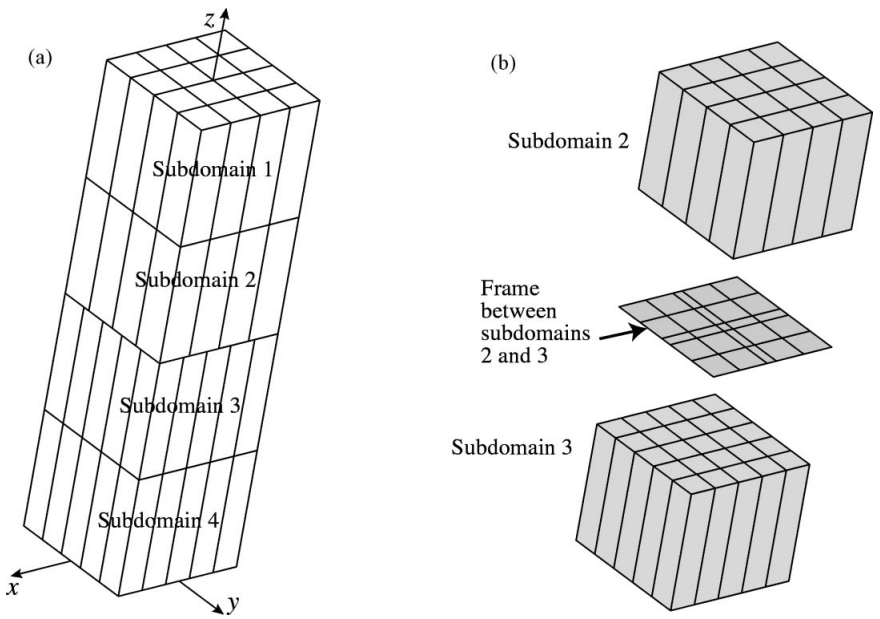

Figure 14. A four-subdomain solid with non-matching brick-element discretizations: (a) partition into four subdomains; (b) colour in subdomains 2 and 3 reflects von Mises stress level while colour in frame reflects its normal displacements.

mesh, the frame nodes coincide with the interface nodes; and similarly for the frame that lies between subdomains 3 and 4. As regards the frame between subdomains 2 and 3, the frame nodes determined by the present frame node placement criterion (25) are located along the x-coordinate at

$$x_b = \langle 0 \;\; 32/140 \;\; 46/100 \;\; 54/100 \;\; 108/140 \;\; 1 \rangle \tag{59}$$

Since the cross-section is square, y_b is likewise determined as shown in Figure 14(b).

The four-subdomain problem is solved by using the partitioned flexibility equation (58). The resulting von Mises stresses are plotted in Figure 14(b) which shows a uniform stress state, thus confirming that a constant stress state is preserved by the present localized interface treatment algorithm. It should be noted that the subdomain-to-global relation matrix for each of the three translational degrees of freedom is given by (48), as discussed in Section 4.3.

6. SUMMARY AND CONCLUSIONS

We have presented an interface treatment that guarantees preservation of the constant-stress interface patch test when the partitioned subdomains are connected. The present method is especially attractive for non-matching interfaces. Once the frame node locations are selected, the frame-to-interface connection matrices can be constructed simply by collocating frame displacements at the partition boundary nodes, avoiding integrations over the interface. This

enhances software modularity when the connected meshes come from different sources and are specified simply in the form of matrices and node locations. The present treatment is variationally based, which insures symmetry. We now summarize the major aspects of this treatment.

(1) The method introduces connection frames between the partitioned domains. A frame is endowed with its own independent displacements and the interface forces acting on it. Hence, this is unique for the three-field as well as the four-field variational framework.
(2) The discrete nodes on the frame are determined by the frame node placement criterion (25) or its specialized form (27). This is a key result of the present paper. Application of the criterion requires only the location of partition boundary nodes and the nodal forces corresponding to constant stress states to be preserved.
(3) The frame nodal placement criterion (25) requires that frame discretization be based on piecewise linear displacements. In the case of general interfaces, the partition boundary nodes are designed to lie along the interpolated frame curve or surface. This alleviates the problem of gaps and interpenetration in problems of contact or in local mesh refinement processes.
(4) From the present treatment it would be possible to devise an equivalent global interface interpolation procedure. While the resulting interface compatibility relations become globally coupled, the relations thus obtained still offer an important advantage: a unique interpolation scheme for the global Lagrange multipliers. To the best of our knowledge, no such algorithm has been previously developed.

Three extensions of the present approach remain largely unexplored. One is interfacing meshes with different degrees of freedom; for example solid domains with nodal translational freedoms only to beam-plate-shell discretizations endowed with nodal rotational degrees of freedom. The second is multiphysics interfacing such as a shell interacting with internal or external fluids. The third is highly irregular grids on both interfaces. Owing to their practical importance in the applications, these extensions deserve further investigation.

ACKNOWLEDGEMENTS

The present work has been supported by Lawrence Livermore National Laboratory under the Scalable Algorithms for Massively Parallel Computations (ASCI level-II) contract B347880, by Sandia National Laboratory under the Accelerated Strategic Computational Initiative (ASCI) contract AS-5666, and by the National Science Foundation under award ECS-9725504.

REFERENCES

1. Lagrange JL. *Mécanique Analytique*, 1788, 1965 Edition complète, 2 vols. Blanchard: Paris, 1965, 44–58.
2. Hallquist JO, Goudreau GL, Benson DJ. Sliding interfaces with contact-impact in large-scale Lagrangian computations. *Computer Methods in Applied Mechanics and Engineering* 1985; **51**:107–137.
3. Simo JC, Wriggers P, Taylor RL. A perturbed Lagrangian formulation for the finite element solution of contact problems. *Computer Methods in Applied Mechanics and Engineering* 1985, **50**:163–180.
4. Taylor RL, Papadopoulos P. On a patch test for contact problems in two dimensions. In *Computational Methods in Nonlinear Mechanics*, Wriggers P, Wagner W (eds). Springer: Berlin, 1991; 690–702.
5. Crisfield MA. Re-visiting the contact patch test. *International Journal for Numerical Methods in Engineering* 2000; **48**:435–449.
6. Aminpour MA, Ransom JB, McCleary SL. A coupled analysis method for structures with independently modelled finite element subdomains. *International Journal for Numerical Methods in Engineering* 1995; **38**:3695–3718.

7. Aminpour MA, Krishnamurthy T, Fadale TD. Coupling of independently modeled three-dimensional finite element meshes with arbitrary shape interface boundaries. *Proceedings of the 1998 AIAA SDM Conference*, Paper No. AIAA 98-2060, 1998; 3014–3024.
8. Brezzi F, Marini D. A three-field domain decomposition method. In *Domain Decomposition Methods in Science and Engineering*, Contemporary Mathematics, vol. 157, Quarteroni A, Periaux J, Kuznetsov YA, Widlund OB (eds). American Mathematical Society: Providence, RI, 1994; 27–34.
9. Bernardi C, Maday Y, Patera AT. A new non-conforming approach to domain decomposition: the mortar element method. *Technical Report*, Université Pierre at Marie Curie, Paris, France, 1990.
10. Belgacem FB, Hild P, Laborde P. Approximation of the unilateral contact problem by the mortar finite element method. *ComptesRendus de L'Académie des Sciences* 1991; **324**:123–127.
11. Bergan PG, Nygård MK. Finite elements with increased freedom in choosing shape functions. *International Journal for Numerical Methods in Engineering* 1984; **20**:643–664.
12. Park KC, Felippa CA. A variational framework for solution method developments in structural mechanics. *Journal of Applied Mechanics* 1998; **65**:242–249.
13. Park KC, Felippa CA. A variational principle for the formulation of partitioned structural systems. *International Journal for Numerical Methods in Engineering* 2000; **47**:395–418.
14. Atluri SN. On 'hybrid' finite-element models in solid mechanics. In *Advances in Computer Methods for Partial Differential Equations*. Vichnevetsky R (ed.). AICA, Rutgers University, New Brunswick, NJ, 1975; 346–356.
15. Tong P. New displacement finite element method for solid continua. *International Journal for Numerical Methods in Engineering* 1970; **2**:73–83.
16. Felippa CA. Parametrized multifield variational principles in elasticity: II. Hybrid functionals and the free formulation. *Communications in Applied Numerical Methods* 1989; **5**:89–98.
17. Felippa CA. A survey of parametrized variational principles and applications to computational mechanics. *Computer Methods in Applied Mechanics and Engineering* 1994; **113**:109–139.
18. Fraeijs de Veubeke BM. *Matrix Structural Analysis*: *Lecture Notes for the International Research Seminar on the Theory and Application of Finite Element Methods*, Calgary, Alberta, Canada, July–August 1973 (reprinted In *B.M. Fraeijs de Veubeke Memorial Volume of Selected Papers*, Geradin M (ed.). Sitthoff & Noordhoff, Alphen aan den Rijn: The Netherlands, 1980; 509–568).
19. Fraeijs de Veubeke BM. Variational principles and the patch test. *International Journal for Numerical Methods in Engineering* 1974; **8**:783–801.
20. Park KC, Felippa CA, Rebel G. Interfacing non-matching finite element discretizations: the zero moment rule. In *Trends in Computational Mechanics*, Wall WA, Bleitzinger K-U, Schweizerhof K (eds). CIMNE: Barcelona, Spain, 2001; 355–367.
21. Rebel G, Park KC, Felippa CA. A contact-impact formulation based on localised Lagrange multipliers, Center for Aerospace Structures. *Report No*. CU-CAS-00-18, University of Colorado, Boulder, CO, July 2000.
22. Felippa CA, Park KC, Justino MR. The construction of free–free flexibility matrices as generalized stiffness inverses. *Computers and Structures* 1998; **68**:411–418.
23. Felippa CA, Park KC. A direct flexibility method. *Computer Methods in Applied Mechanics and Engineering* 1997; **149**:319–337.
24. Justino MR, Park KC, Felippa CA. An algebraically partitioned FETI method for parallel structural analysis: implementation and numerical performance evaluation. *International Journal for Numerical Methods in Engineering* 1997; **40**:2739–2758.
25. Park KC, Justino MR, Felippa CA. An algebraically partitioned FETI method for parallel structural analysis: algorithm description. *International Journal for Numerical Methods in Engineering* 1997; **40**:2717–2737.
26. Gumaste U, Park KC, Alvin KF. A family of implicit partitioned time integration algorithms for parallel analysis of heterogeneous structural systems. *Computational Mechanics Journal* 2000; **24**:463–475.
27. Park KC, Reich GW, Alvin KF. Damage detection using localized flexibilities. In *Structural Health Monitoring, Current Status and Perspectives*, Chang F-K (ed.). Technomic Pub., CRC Press, Boca Raton, FL, 1997; 125–139.
28. Park KC, Reich GW. A theory for strain-based structural system identification. *Proceedings of the 9th International Conference on Adaptive Structures and Technologies*. Cambridge, MA, 14–16 October 1998.
29. Park KC, Felippa CA. A flexibility-based inverse algorithm for identification of structural joint properties. Proceedings of the *ASME Symposium on Computational Methods on Inverse Problems*, Anaheim, CA, 15–20 November 1998.
30. Park KC, Kim NI. A theory of localized vibration control via partitioned LQR synthesis, Center for Aerospace Structures. Report No. CU-CAS-98-13, University of Colorado, Boulder, CO, July 1998. *Proceedings XXI Congresso Nacional de Matematica Applicada e Computacional*, Caxambu, MG, Brazil, September 1998.

